

**Josephson coupling in the dissipative state of a thermally hysteretic  $\mu$ -SQUID**Sourav Biswas,<sup>1</sup> Clemens B. Winkelmann,<sup>2</sup> Hervé Courtois,<sup>2</sup> and Anjan K. Gupta<sup>1,\*</sup><sup>1</sup>*Department of Physics, Indian Institute of Technology Kanpur, Kanpur 208016, India*<sup>2</sup>*Univ. Grenoble Alpes, CNRS, Grenoble INP, Institut Néel, 38000 Grenoble, France*

(Received 14 September 2017; revised manuscript received 21 November 2017; published 27 November 2018)

Micron-sized superconducting interference devices ( $\mu$ -SQUIDs) based on constrictions optimized for minimizing thermal runaway are shown to exhibit voltage oscillations with applied magnetic flux despite their hysteretic behavior. We explain this remarkable feature by a significant supercurrent contribution surviving deep into the resistive state due to efficient heat evacuation. A resistively shunted junction model, complemented by a thermal balance determining the amplitude of the critical current, describes well all experimental observations, including the flux modulation of the (dynamic) retrapping current and voltage, by introducing a single dimensionless parameter. Compared to the nonhysteretic regime, this regime extends the voltage readout mode in a given  $\mu$ -SQUID to further lower temperatures. More importantly, the quantitative modeling of this regime incorporating both heating and phase dynamics paves the way for further optimization of  $\mu$ -SQUIDs for nanomagnetism.

DOI: [10.1103/PhysRevB.98.174514](https://doi.org/10.1103/PhysRevB.98.174514)**I. INTRODUCTION**

A superconducting quantum interference device (SQUID), in which two Josephson junctions (JJs) form a closed loop, exhibits a modulation of the critical current  $I_c$  as a function of the magnetic flux through the loop with a period  $\Phi_0 = h/2e$ . It is the most sensitive magnetic field transducer to date [1,2]. Miniaturized SQUIDs have been used for probing magnetic properties of nanoparticles [3–6] and surfaces with submicron resolution [7,8]. The coupling of a nanoparticle's magnetic flux to a  $\mu$ - or nano-SQUID is far better [1] than coupling it to a conventional SQUID, leading to a magnetic moment resolution down to below  $1 \mu_B$  [4,9]. Thus, optimizing such  $\mu$ -SQUIDs in terms of sensitivity, ease of fabrication, and operation or operating temperature and magnetic field range is the focus of a large number of recent works [10–16]. However, hysteresis in the current-voltage characteristics (IVCs) of  $\mu$ -SQUIDs severely limits their flux resolution and speed. Hysteresis in conventional SQUIDs based on superconductor-insulator-superconductor Josephson junctions is well understood in the frame of the resistively and capacitively shunted junction (RCSJ) model [17,18]. In contrast, hysteresis in weak-link (WL)-based  $\mu$ -SQUIDs arises from the Joule heating leading to a self-sustained hot spot [19–22].

Despite their hysteresis, Nb-based  $\mu$ -SQUIDs have been remarkably successful in nano-magnetism, in particular in the pioneering works of Wernsdorfer and collaborators [3–5]. Their fabrication based on electron lithography is easy and scalable. Efforts to fabricate high-sensitivity nano-SQUIDs based on high- $T_c$  cuprate films have also been quite successful recently [23–25]. Nevertheless, all WL-based SQUIDs exhibit hysteresis at very low temperatures, where the quantum dynamics of magnetization can be probed. Hence, ways to

further optimize Nb-based  $\mu$ -SQUIDs down to very low temperatures with high speed and sensitivity are being investigated [26–28]. A hurdle in this direction is the poor understanding of the phase-dynamic regime in WLs due to the contribution of heating and other nonequilibrium effects. Only in this dynamic regime can a SQUID exhibit voltage oscillations with magnetic flux, making the fast voltage-readout-mode possible. The latter uses the linear portion of the voltage response to flux at fixed bias current in order to operate a SQUID in a flux-locked loop [17].

In a WL biased with a current  $I$  close to the critical current  $I_c$ , the transition to the dissipative state is triggered by a phase slip [29,30], which changes  $\varphi$  between the leads by  $2\pi$ . The ensuing voltage peak, and thus heating, generally suffices to create an avalanche of phase slips, driving the local WL temperature  $T_{WL}$  above the bath temperature  $T_b$ . When the bias current is ramped down, superconductivity is recovered only at the so-called retrapping current ( $< I_c$ ), leading to hysteresis. The hot-spot model by Skocpol, Beasley, and Tinkham (SBT) [19] considers that in the finite-voltage state the temperature  $T_{WL}$  is above the critical temperature  $T_c$ . The Josephson coupling is then lost, so that no SQUID-type behavior is observed in this state for most of the temperature range [22,31,32]. Still, it has been observed in some devices based on WLs [20,33,34] and superconductor-normal metal-superconductor (SNS) junctions [35–37]. In most cases, the theoretical modeling neglected thermal effects and relied on a conventional RCSJ model, but with an effective capacitance [38] well above the actual geometric one. Eventually, the SBT model was also extended to the case of a WL temperature remaining below  $T_c$ , still ignoring the WL phase dynamics [33,34].

Recently, some of us proposed a dynamic thermal model [39] of WLs, incorporating both the overheating of the WL at a temperature  $T_{WL}$  and a resistively shunted junction (RSJ)-type phase dynamics. If  $T_{WL}$  remains below  $T_c$ , then the Josephson coupling across the WL is not fully destroyed.

\*anjankg@iitk.ac.in

The Josephson current, together with the normal current, persists over a portion of the finite-voltage branch of the IVCs [40], thus leading to SQUID-type voltage oscillations. This dynamic thermal model (DTM) is in between the SBT model, where the Josephson coupling does not exist at nonzero voltages, and the R(C)SJ model that ignores the thermal effects. A similar approach was used to describe the radio-frequency response of a SNS junction [41]. Alternatively, hysteresis in the phase-slip-controlled regime can be described using a more elaborate nonequilibrium approach using time-dependent Ginzburg-Landau equations [42].

In this paper, we report temperature- and magnetic-field-dependent transport in  $\mu$ -SQUIDS with a geometry optimized for a moderate Joule heating. Despite being clearly hysteretic, the devices exhibit voltage oscillations with the magnetic flux. The related nonzero flux-sensitive supercurrent contribution surviving well above the critical current and within a finite current window, which cannot be understood using either the static SBT or isothermal R(C)SJ model, is analyzed with the dynamic thermal model, which quantitatively captures every observation. We eventually discuss the flux sensitivity of the studied hysteretic  $\mu$ -SQUIDS in the dynamic regime.

## II. DYNAMIC THERMAL MODEL

In the dissipative state, phase slips [30,43,44] occur at a rate  $V/\Phi_0 \simeq \tau_J^{-1} = R_N I_c^0 / \Phi_0$ , where  $I_c^0$  is the zero-magnetic-field critical current, taken here at the bath temperature. Each phase slip deposits a Joule heat  $I\Phi_0$ , leading to a temperature rise in the WL region. The Joule heat is generated over a length scale determined by the inelastic quasiparticle diffusion length [45,46], much longer than the WL dimensions studied here. Thus we assume a uniform [30] temperature over the entire WL, which determines its critical current  $I_c$ . The characteristic time for the thermal balance is  $\tau_{th} = C_{WL}/k$ , where  $C_{WL}$  is the WL heat capacity and  $k$  is the thermal conductance to the bath. Under the quasistatic approximation, the instantaneous WL temperature  $\mathcal{T}_{WL}$  is dictated by a thermal balance between the Joule heat and the conduction to the bath  $k(\mathcal{T}_{WL} - T_b)$ .

If the temperature  $\mathcal{T}_{WL}$  remains below  $T_c$  at any instant of time  $t$ , the bias current  $I$  is dynamically shared between a supercurrent  $\mathcal{I}_s(t)$  and a complementary normal current. This gives rise to a time-dependent voltage  $\mathcal{V}(t) = R_N[I - \mathcal{I}_s(t)]$  related to the phase difference  $\varphi$  through the Josephson relation  $\mathcal{V}(t) = \Phi_0 \dot{\varphi} / 2\pi$ . The heat balance equation governing the dynamics of temperature is written as  $C_{WL} \dot{\mathcal{T}}_{WL} + k(\mathcal{T}_{WL} - T_b) = \mathcal{V}^2(t) / R_N$ . These two equations can be rearranged in terms of dimensionless variables as [39]

$$\dot{\varphi} = 2\pi(i - i_s), \quad (1)$$

$$\alpha \dot{p} + p = \frac{\beta}{4\pi^2} \dot{\varphi}^2. \quad (2)$$

Here the currents  $i$  and  $i_s$  are, respectively, the currents  $I$  and  $\mathcal{I}_s$  in units of the zero-magnetic-field critical current  $I_c^0(T_b)$ . The time unit is  $\tau_J$ , and  $\alpha = \tau_{th}/\tau_J$ . The dimensionless

temperature is defined as

$$p = \frac{\mathcal{T}_{WL} - T_b}{T_c - T_b}. \quad (3)$$

We also define the dimensionless parameter

$$\beta = \frac{R_N I_c^{02}(T_b)}{k(T_c - T_b)} \quad (4)$$

as the ratio of Joule heat generation (at  $I_c^0$ ) and heat evacuation (at  $T_c$ ).

The static retrapping current  $I_h$  [47] is defined by the WL being right at the critical temperature ( $\mathcal{T}_{WL} = T_c$ ). From Eq. (2), the thermal balance  $k(\mathcal{T}_{WL} - T_b) = R_N I^2$  gives

$$I_h = I_c^0 / \sqrt{\beta}. \quad (5)$$

At a larger current  $I > I_h$  we have  $\mathcal{T}_{WL} > T_c$ , so that there is no Josephson coupling, and hence,  $V = R_N I$ . A nonzero supercurrent can be carried by the WL only for  $I < I_h$ .

The dynamic retrapping current  $I_r^{\text{dyn}}$  is the current below which the dynamic state ceases to exist and the zero-voltage state becomes stable against any phase slip. Here and in the following, we consider WLs featuring a linear temperature dependence of the critical current and a sinusoidal current-phase relation  $\mathcal{I}_s(\varphi)$ . One can then obtain by solving Eqs. (1) and (2) [39]

$$2\beta^2 \left[ \frac{I_r^{\text{dyn}}}{I_c^0} \right]^2 = \sqrt{1 + 4\beta^2} - 1. \quad (6)$$

From numerical simulations, we find that a nonsinusoidal  $\mathcal{I}_s(\varphi)$ , within a regime of single-valued current, negligibly affects this relation. Moreover, the elevated WL temperature in the dynamic state gives rise to an increase in coherence length  $\xi$ , and thus, the current-phase relation  $\mathcal{I}_s(\varphi)$  is close to sinusoidal.

The extent of the dynamic regime, defined by the current bias window  $I_r^{\text{dyn}} < I < I_h$ , depends on the value of the dimensionless parameter  $\beta$ . Figure 1(a) depicts the device state diagram found using the  $\beta$  dependence of  $I_r^{\text{dyn}}$  and  $I_h$ . For large values of  $\beta$ , i.e., poor heat evacuation and/or high  $I_c^0$ ,  $I_r^{\text{dyn}}$  and  $I_h$  are both below  $I_c^0$  and very close to each other. The dynamic regime then occurs in a bias current window of vanishing width, making its observation in IVCs practically impossible [27,31]. In this limit, the physics is well described by the SBT and other static thermal models [19,20,31]. In contrast, for  $\beta$  of about unity or smaller, the dynamic regime spans a significant current range. The static retrapping current  $I_h$  can then significantly exceed  $I_c^0$ , and the dynamic retrapping current  $I_r^{\text{dyn}}$  is close to  $I_c^0$ . For extremely good heat evacuation  $\beta \rightarrow 0$ , one has  $I_h \rightarrow \infty$  and  $I_r^{\text{dyn}} \rightarrow I_c^0$ , and RSJ model is recovered.

In the dynamic regime between  $I_r^{\text{dyn}}$  and  $I_h$ , the WL temperature  $\mathcal{T}_{WL}$  oscillates with time about an average value. However, for a large value of  $\alpha$ , the magnitude of these oscillations is negligible compared to the average WL temperature [39]. This is always the case as  $\tau_{th}$ , which can range from tens of nanoseconds to microseconds, is greater than  $\tau_J$ , which is of picosecond order. The WL can thus be considered at

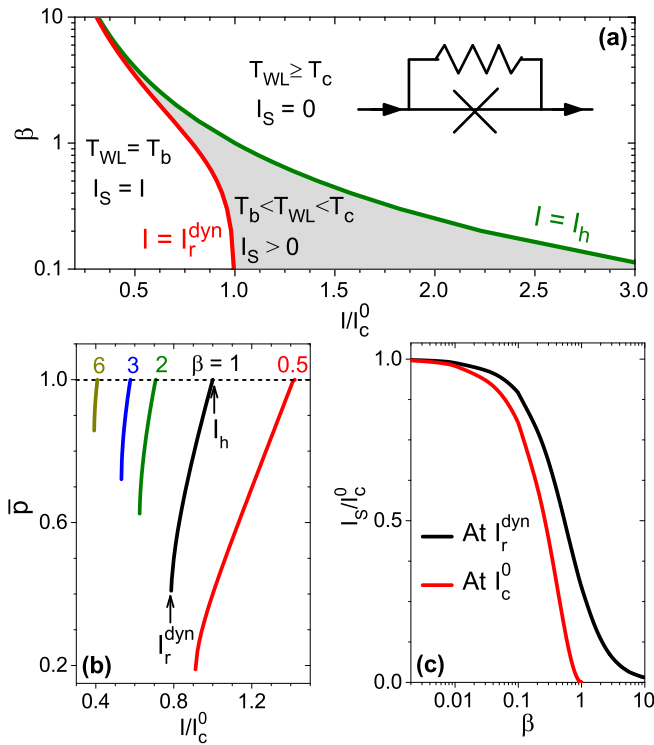


FIG. 1. Device state diagram with the gray shaded region indicating the dynamic regime where the WL has a finite voltage but carries a nonzero supercurrent. The region to the left of this gray region is the zero-voltage state where all the bias current is carried as supercurrent, while the right region has no supercurrent. The red (green) line depicts the  $\beta$  dependence of  $I_r^{\text{dyn}}$  ( $I_h$ ). Inset: Equivalent circuit of the DTM. (b) Variation of the dimensionless time-averaged WL temperature  $\bar{\beta}$  with the bias current in the dynamic regime for different  $\beta$  values. (c) Ratio of the time-averaged supercurrent  $I_s$  and the critical current  $I_c^0$  as a function of  $\beta$  at the bias current values of  $I_r^{\text{dyn}}$  and  $I_c^0$ .

a constant (time-averaged) temperature  $T_{\text{WL}}$  [30,39,41]. The corresponding time-averaged reduced temperature  $\bar{\beta}$  can be calculated as a function of the current bias  $i$  from Eqs. (1) and (2) [39]:

$$\bar{\beta} = \frac{i^2 \beta^2 + \sqrt{-i^2 \beta^2 + i^4 \beta^2 + i^6 \beta^4}}{1 + i^2 \beta^2}, \quad (7)$$

with  $\beta$  being the single parameter. Figure 1(b) shows how  $\bar{\beta}$  (or, equivalently,  $T_{\text{WL}}$ ) decreases with the current bias for various values of the parameter  $\beta$ , starting from 1 (or  $T_c$ ) at  $I_h$ . At every bias, one can thus calculate the critical current  $I_c(T_{\text{WL}})$  and the related time-averaged voltage as

$$V = R_N \sqrt{I^2 - I_c^2(T_{\text{WL}})} \quad (8)$$

and the time-averaged supercurrent  $I_s$  as

$$I_s = I - V/R_N = I - \sqrt{I^2 - I_c^2(T_{\text{WL}})}. \quad (9)$$

Figure 1(c) shows  $I_s$  as a function of the parameter  $\beta$  at bias current values equal to  $I_r^{\text{dyn}}$  and  $I_c^0$ . For  $\beta > 1$ , the time-averaged supercurrent  $I_s$  is zero when the bias current reaches  $I_c^0$  [19,31]. In practice, as soon as  $\beta$  exceeds about 2,

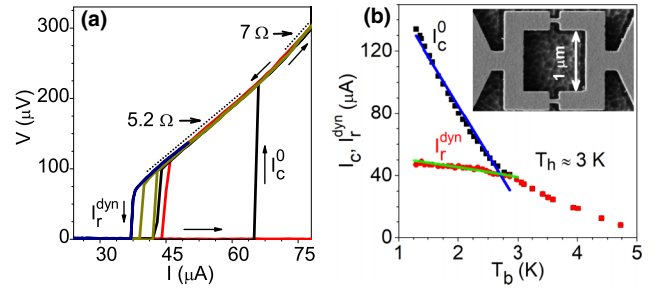


FIG. 2. (a) Current-voltage characteristics at different temperatures in the hysteretic regime. Red, black, green, and blue correspond to  $T_b = 1.67, 2.27, 2.77,$  and  $2.98$  K, respectively. (b) Temperature dependence of the critical current  $I_c^0$  and the (dynamic) retrapping current  $I_r^{\text{dyn}}$ . The crossover temperature  $T_h$  is close to 3 K. The solid lines are fits below  $T_h$ . The critical current  $I_c^0$  is fit to  $211.2(1 - T_b/3.3)$ , which gives the zero-temperature critical current  $I_{c0} = 211.2 \mu\text{A}$ . The dynamic retrapping  $I_r^{\text{dyn}}$  is fit to Eq. (6), which gives the WL critical temperature  $T_c = 6.0$  K. Inset: Scanning electron micrograph of the SQUID loop.

the WL switches almost immediately to a fully normal state with  $T_{\text{WL}} \geq T_c$  and (almost) zero supercurrent. For small  $\beta$  values, the supercurrent  $I_s$  is comparable to the full critical current  $I_c^0$ .

### III. EXPERIMENTAL DETAILS

The fabrication of the  $\mu$ -SQUIDs starts with the deposition of a Nb thin film with a thickness of 40 nm on a Si substrate. A resist layer was afterwards patterned using laser lithography for the outer leads and contact pads and electron-beam lithography for the smaller structures. A 25-nm-thick Al layer was then deposited, followed by liftoff. With the latter acting as a protective mask, the Nb devices were obtained by a  $\text{SF}_6$  reactive-ion etch. The Al mask is eventually chemically etched. Figure 2(b) shows the loop of a SQUID with the two constrictions, with nominal width and length of 40 and 160 nm, respectively, in parallel. The critical current  $I_c$  was tuned down (to the  $100 \mu\text{A}$  range) by trimming [28] down the Nb thickness to  $20 (\pm 2)$  nm in subsequent reactive-ion etching steps without an Al mask. The etching process can also lead to a reduction in  $T_c$  due to the appearance of a nonsuperconducting layer on the top and bottom and also on the sides [48–50]. However, the thickness of such a layer [51,52] is estimated to be only  $\sim 2$  nm, which leaves a large and effective superconducting channel at the core of the WLs.

Electrical transport measurements were carried out in a closed-cycle refrigerator with a base temperature of 1.3 K. The electrical signals are thoroughly filtered, both at room temperature ( $\pi$  filters) and at base temperature (copper-powder filters). Home-made ground-isolated current sources and voltage amplifiers were used. From the temperature-dependent four-probe transport measurements of the first device, we find the onset of superconductivity at 8.6 K and a sheet resistance  $R_{\square} = 5.8 \Omega$  in the normal state. In the following, we will present experimental data mainly from one sample. Another sample featured a similar behavior (see Appendix A).

#### IV. RESULTS

Zero-field IVCs of a  $\mu$ -SQUID at various bath temperatures  $T_b$  are shown in Fig. 2(a). The critical current  $I_c^0$  varies strongly with temperature and exceeds  $100 \mu\text{A}$  below 2 K [see Fig. 2(b)]. The critical current density  $J_c$  at 1.3 K, found as  $21.1 \text{ MA/cm}^2$ , is close to the Ginzburg-Landau depairing current density  $J_{dp} = (2/3)^{3/2}[H_c(0)/\lambda] = 36 \text{ MA/cm}^2$  (at zero temperature), estimated using parameters for bulk and clean Nb [18]. This  $J_c$  value is similar to that of our earlier devices [31]. Together with the linear dependence (up to  $T_h$ ) of the critical current  $I_c^0$  on the bath temperature  $T_b$ , this confirms the intrinsic superconducting nature of the WLs as opposed to that of SNS WLs [31,41,53]. Below the crossover temperature  $T_h \approx 3 \text{ K}$ , hysteresis is observed with a retrapping to the zero-resistance state at a well-defined *dynamic* retrapping current  $I_r^{\text{dyn}}$  [39] [see Fig. 2(a)]. A fit of its temperature dependence to Eq. (6) provides the value for the critical temperature of the WL  $T_c = 6.0 \text{ K}$ . At bias currents significantly above  $I_c^0$ , further thermal instabilities occur in larger portions of the device, as evidenced by additional retrapping currents (see Appendix A). Our study here is focused on the hysteretic regime and at bias currents below or in the vicinity of the critical current  $I_c$ .

In the dissipative branch, the IVC slope  $dV/dI$  varies with the bias current from  $5.2 \Omega$  (just above  $I_r^{\text{dyn}}$ ) to  $7 \Omega$  (above  $I_c^0$ ) at 1.67 K [see Fig. 2(a)]. In the low-bias regime of interest here, the differential resistance is always close to  $R_N = 5.2 \Omega$  independent of bias current and temperature (see Appendix A). This value is significantly below the value of  $11.5 \Omega$  for the resistance of two WLs in parallel estimated from the sheet resistance. This indicates that the WLs are not fully resistive in this dissipative state.

When applying a perpendicular magnetic field  $B$  and thus a flux  $\Phi = BS$ , the critical current  $I_c$  displays a  $\Phi_0$ -periodic modulation, taking an effective SQUID loop area  $S = 1.6 \mu\text{m}^2$ . The flux modulation of the critical current, starting from its maximal zero-field value  $I_c^0$ , is not complete and has a rather triangular shape [see Figs. 3(a) and 3(b)]. This behavior cannot be explained solely by asymmetric critical currents between the two arms. Moreover, self-flux-related effects [17], related to the loop inductance  $L$ , are negligible here, as we estimate  $LI_c^0/\Phi_0 < 0.1$ . For a WL with a length  $\ell \geq \xi$ , the supercurrent phase  $\mathcal{I}_s(\varphi)$  relation is nonsinusoidal [54–57]. Numerical calculations using a nonsinusoidal  $\mathcal{I}_s(\varphi)$  relation indeed yield an incomplete cancellation of  $I_c$  at  $\Phi = \Phi_0/2$  (Appendix B), similar to the experimental behavior.

Strikingly, the retrapping current  $I_r^{\text{dyn}}$  also shows oscillations with the magnetic flux [see Figs. 3(a) and 3(b)], in contradiction to the SBT picture of a fully normal state of the device in the dissipative state. A similar feature was observed in SQUIDs based on normal-metal WLs [35–37] but not satisfactorily explained. It constitutes the first indication that superconductive coupling is not fully suppressed by the electron heating in the dissipative branch of our hysteretic devices.

Moreover, the SQUID voltage also shows an oscillatory dependence on magnetic field for a wide bias current window [see Figs. 3(c)–3(f)]. This is completely opposed to the SBT model behavior, in which the dissipative state displays no signature of Josephson coupling across the SQUID WLs. The

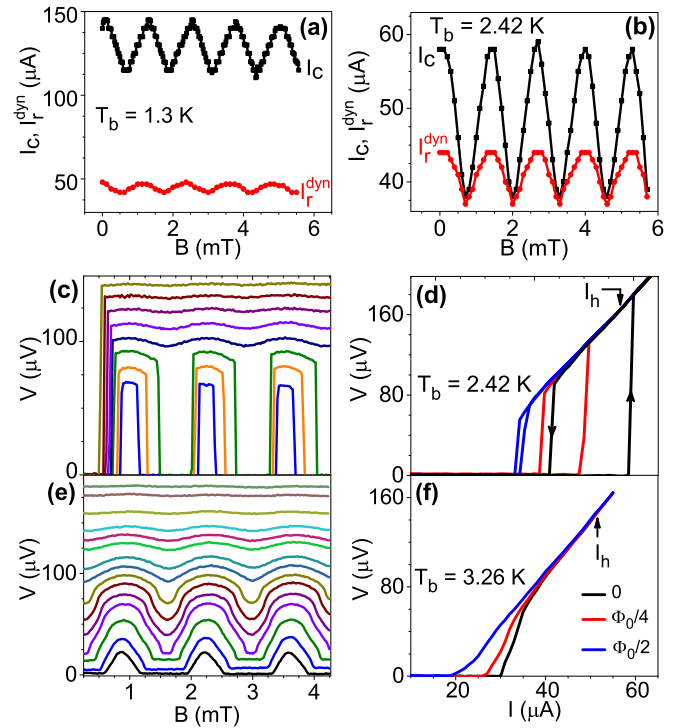


FIG. 3. (a) and (b) Oscillations of the critical and dynamic retrapping currents with the magnetic field in the hysteretic regime at 1.3 and 2.42 K, respectively. (c) Voltage oscillation with magnetic field for  $I = 39$  to  $53 \mu\text{A}$  in  $2 \mu\text{A}$  intervals at 2.42 K. (e) The same for  $I = 25$  to  $50 \mu\text{A}$  at 3.26 K. (d) and (f) IVCs at different flux values ( $0$ ,  $\Phi_0/2$ , and  $\Phi_0/4$ ) at 2.42 and 3.26 K, respectively.

initial jump in voltage, seen for  $I_r^{\text{dyn}} < I < I_c$  [see Fig. 3(c)], occurs due to the first arrival to the resistive branch. At a fixed temperature, the IVCs at different flux values are found to merge on the linear branch [see Figs. 3(d) and 3(f)], beyond a particular bias current. We identify this current as the *static* retrapping current  $I_h$  [39], as discussed in Sec. II. The  $V$ - $B$  oscillations consistently disappear at a bias current beyond  $I_h$ . At lower temperatures ( $T_b = 1.3$  and  $2 \text{ K}$ ) in the hysteretic regime,  $V$ - $B$  oscillations are observed over a narrow bias current span just above  $I_r^{\text{dyn}}$  [see Figs. 4(a) and 4(b)].

The flux-to-voltage transduction function  $V_\Phi$ , defined as the maximum of  $\partial V/\partial \Phi(\Phi)$ , is found to be  $27 \mu\text{V}/\Phi_0$  in

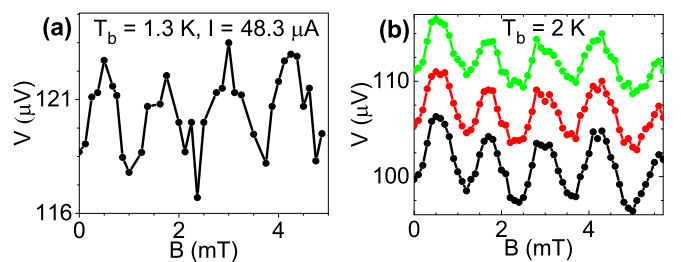


FIG. 4. (a)  $V$ - $B$  oscillation at the lowest temperature of 1.3 K at a bias current of  $48.3 \mu\text{A}$  just above the dynamic retrapping current  $I_r^{\text{dyn}}$ . (b) Same at 2 K for three different bias currents (45, 46, and  $47 \mu\text{A}$ ) very close to  $I_r^{\text{dyn}}$ . At these lower temperatures, voltage values are extracted from IVCs at different magnetic field values.

the dynamic regime at  $T_b = 2.42$  K. With a voltage noise of  $\sim 1$  nV/ $\sqrt{\text{Hz}}$  in our circuit, this gives a flux noise density  $\sqrt{S_\Phi} \approx 37 \mu\Phi_0/\sqrt{\text{Hz}}$ . In the nonhysteretic regime, thanks to higher flux-to-voltage transduction  $V_\Phi$ , the sensitivity  $\sqrt{S_\Phi}$  reaches  $3 \mu\Phi_0/\sqrt{\text{Hz}}$  at  $T_b = 3.26$  K. The latter value is similar to the ones reported in nonhysteretic  $\mu$ -SQUIDs with room-temperature amplifiers [1,58].

## V. DISCUSSION

To model the  $\mu$ -SQUID, we assume the WLs are identical, with a temperature-dependent critical current  $I_c^0/2$ , a temperature-independent normal-state resistance  $2R_N$ , and a heat-loss coefficient  $k/2$ . The two WLs' phases,  $\varphi_1$  and  $\varphi_2$ , maintain a constant difference,  $\varphi_1 - \varphi_2 = 2\pi\Phi/\Phi_0$ , forced by the magnetic flux through the SQUID loop. Consequently, the two WLs' average temperatures are identical in the dynamic steady state. Eventually, the SQUID behaves as a single WL with normal resistance  $R_N$ , heat-loss coefficient  $k$ , and critical current  $I_c(T_{\text{WL}}, \Phi) = I_c^0(T_{\text{WL}}) |\cos(\pi\Phi/\Phi_0)|$ . The flux modulation of the critical current alters the expression for the dynamic retrapping current to

$$\frac{I_r^{\text{dyn}}(\Phi)}{I_c^0} = \frac{\sqrt{\sqrt{1 + 4\beta^2 \cos^4(\pi\Phi/\Phi_0)} - 1}}{\sqrt{2}\beta |\cos(\pi\Phi/\Phi_0)|}. \quad (10)$$

At zero flux, this expression matches Eq. (6). In the limit of a small  $\beta$ , one recovers the usual  $|\cos(\pi\Phi/\Phi_0)|$  modulation. In contrast,  $I_h$  is independent of the flux.

For every bath temperature, we use Eq. (6) of the DTM with the measured zero-flux dynamic retrapping current  $I_r^{\text{dyn}}$  and critical current  $I_c^0$  to extract the value of  $\beta$ . Figure 5(a) shows how the parameter  $\beta$  varies with the bath temperature  $T_b$  over the hysteretic regime, from close to zero at  $T_h$  to about 8 at 1.3 K. For small  $\beta$  values,  $I_r^{\text{dyn}}$  and  $I_c^0$  are (almost) indistinguishable in IVCs. Thus, the error bars in  $\beta$  increase when  $T_b$  is increased towards  $T_h$  [see Fig. 5(a)], and the method cannot be used beyond that. As discussed below, the variation of the residual supercurrent with the bias current is then a more appropriate method to extract the value of  $\beta$ . With the temperature coefficient of the measured critical current  $I_c^0(T_b)$  below  $T_h$  being known [see Fig. 2(b)], we use Eq. (4) with  $k$  as the single free parameter to fit the  $\beta(T_b)$  curve. We obtain  $k = 2.6$  nW/K. Alternatively, we can also use the value of  $I_{c0}^2 R_N/kT_c = 13.9$  obtained from the fit of the dynamic retrapping current as a function of the bath temperature  $I_r^{\text{dyn}}(T_b)$ , which gives  $k \approx 2.8$  nW/K. Using a typical value of the heat-transfer coefficient such as  $5 \text{ W/cm}^2 \text{ K}$  [22,31] and these two close values of  $k$ , the effective heat-loss area is estimated to be  $\sim 0.06 \mu\text{m}^2$ , which is larger than but still comparable to the  $0.16 \times 0.04 \mu\text{m}^2$  area of the WL.

Using the variation of the parameter  $\beta$  as a function of the bath temperature  $T_b$ , Eq. (7) provides us with the behavior of the WL temperature  $T_{\text{WL}}$  at a bias current equal to the corresponding dynamic retrapping current  $I_r^{\text{dyn}}$  [see Fig. 5(a)]. At the crossover temperature  $T_h$  where  $\beta$  is small, the WL is at thermal equilibrium with the bath, i.e.,  $T_{\text{WL}} \approx T_b$ , as in

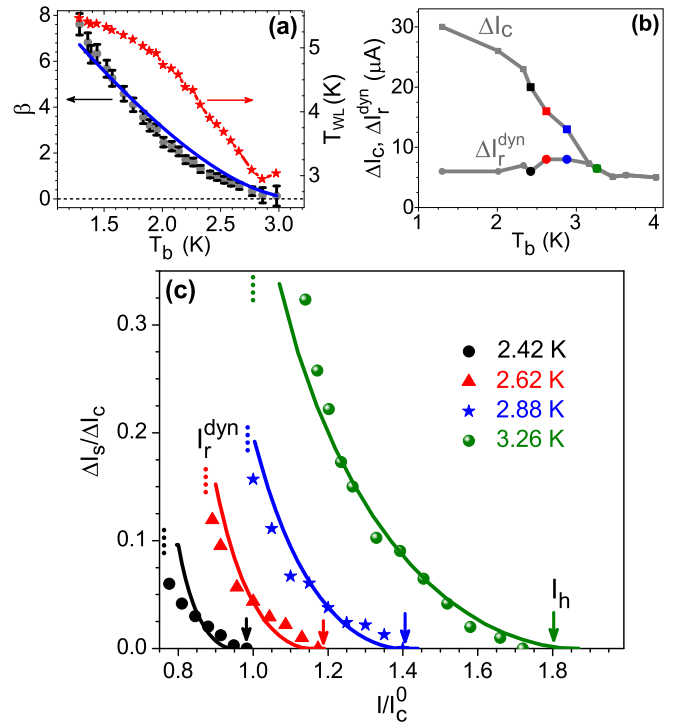


FIG. 5. (a) Gray symbols: change in  $\beta$  with bath temperature for the measured first device as found using  $I_r^{\text{dyn}}$  and  $I_c^0$  in the hysteretic regime (below  $T_h \simeq 3$  K). The blue solid line is a fit per Eq. (4) in DTM with  $k = 2.6$  nW/K. Red symbols and line represent the WL temperature  $T_{\text{WL}}$  as a function of the bath temperature  $T_b$  and at a bias current equal to the corresponding  $I_r^{\text{dyn}}$ . (b) Variation of the modulation amplitudes  $\Delta I_c$  and  $\Delta I_r^{\text{dyn}}$  with bath temperature. (c) Symbols: measured supercurrent modulation amplitude in units of the critical current modulation amplitude  $\Delta I_s/\Delta I_c$  in the dissipative state as a function of bias current ranging from  $I_r^{\text{dyn}}$  to  $I_h$  at different bath temperatures. Solid lines: best fit to the DTM with fit parameters listed in Table I. The value of  $I_c^0$ , setting the  $x$ -axis scale, depends on the bath temperature. Arrows and dotted lines indicate the positions of the static and dynamic retrapping current  $I_h$  and  $I_r^{\text{dyn}}$ , respectively.

the isothermal RSJ model. Towards low temperature, the WL temperature  $T_{\text{WL}}$  increases towards  $T_c$ .

A small  $\beta$  value, required for observation of the dynamic regime, necessitates a small critical current  $I_c$  and/or a large thermal conductance to the bath  $k$ . Compared to earlier similar devices [31] for which we estimate  $\beta$  to be about 20 at 4.2 K, we enhanced  $k$  by widening the leads right outside the SQUID loop while still keeping a short and narrow neck between the SQUID loop and the wide leads to avoid vortices between the two WLs' current path [59]. As described earlier, we reduced  $I_c$  approximately by an order of magnitude by trimming the Nb thickness down, which overall dominates the decrease in  $\beta$  value. The value  $\beta = 2$  obtained at 2.1 K [see Fig. 5(a)] approximately defines the low-temperature limit for practical operation of the SQUID in the voltage-modulation mode, significantly below the hysteresis temperature  $T_h$ . At lower temperatures, the bias-current range of the dynamic regime is narrow, and the voltage oscillations are of small amplitude.

TABLE I. Sample parameters, including the calculated and fitted values of  $\beta$  for different temperatures.

$T_b$ (K)	$I_c^0$ ( $\mu\text{A}$ )	$I_r^{\text{dyn}}$ ( $\mu\text{A}$ )	$\beta$ from $I_r^{\text{dyn}}$ value	$\beta$ from Fig. 5 fit
2.42	58	44	1.13	1.1
2.62	46	40	0.66	0.74
2.88	40	38	0.35	0.5
3.26	31.6	31.6		0.28

In the experiment and as discussed above, the critical current is not fully modulated by the flux, which implies the same for the supercurrent. Thus, one cannot compare the supercurrent calculated from the model directly to the one deduced from the measured voltage oscillations. We consider the amplitude of the supercurrent modulation in units of the critical current modulation by the flux, i.e.,  $\Delta I_s/\Delta I_c$ . From the experimental data, we calculate  $\Delta I_s/\Delta I_c$  as being equal to  $\Delta V/(R_N \Delta I_c)$ , where  $\Delta V$  and  $\Delta I_c$  are the modulation amplitudes of the voltage and the critical current, respectively. As for the theory, we calculate

$$\frac{\Delta I_s}{\Delta I_c} = \frac{I - \sqrt{I^2 - I_c^0(T_{\text{WL}})}}{I_c^0(T_b)}, \quad (11)$$

with the temperature  $T_{\text{WL}}$  being found using Eq. (7), with  $\beta$  being the single adjustable parameter.

Figure 5(c) shows the experimental (symbols) and theoretical (lines) values of the ratio  $\Delta I_s/\Delta I_c$  as a function of the normalized bias current capturing most of the dynamic regime. Very good quantitative agreement is obtained. The fit values of  $\beta$  listed in Table I agree well with those deduced and plotted in Fig. 5(a) from the analysis of the dynamic retrapping current. The comparison made here is fully justified only in the case of a sinusoidal  $I_s(\varphi)$ . Extending this to the case of a nonsinusoidal current-phase relation is intuitive but still not fully theoretically established. Still, the successful comparison of experimental data and theoretical calculation demonstrates that the DTM accurately describes the transition between the isothermal Josephson junction behavior and the electronically overheated and hysteretic  $\mu$ -SQUID behavior. We attribute a small discrepancy in fits to the assumptions made in the model, such as the temperature independence of the thermal parameters.

The insights gained from the above study, in particular the key role of the parameter  $\beta$ , provide a guideline for designing devices with improved performance. While for  $0.4 < \beta < 2$  a wide dynamic regime is obtained, featuring both hysteretic behavior and SQUID voltage oscillations, one needs to reach  $\beta < 0.4$  so that hysteresis disappears and the voltage modulations reach a significant fraction of  $\Delta/e$ . This is illustrated for a device in Fig. 6, with narrower WLs compared to the previous one, resulting in a smaller critical current  $I_c$  and thus a small  $\beta \sim 0.36$ , even at 1.3 K.

In this device, the flux-to-voltage transduction function  $V_\Phi$  is 1 mV/ $\Phi_0$  at 1.3 K. With an estimated voltage noise of 1 nV/ $\sqrt{\text{Hz}}$  in our circuit, we find a flux noise density  $\sqrt{S_\Phi} \approx 1 \mu\Phi_0/\sqrt{\text{Hz}}$ , i.e., significantly below the values of  $3 \mu\Phi_0/\sqrt{\text{Hz}}$  previously reported in nonhysteretic  $\mu$ -SQUIDS

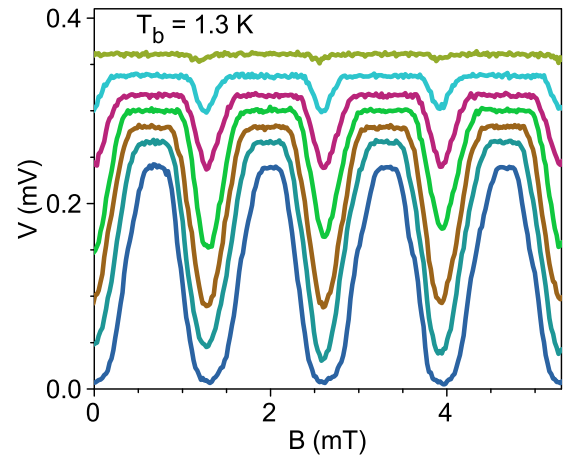


FIG. 6.  $V$ - $B$  oscillations of another device with a small critical current  $I_c^0 = 51 \mu\text{A}$  and thus a small  $\beta = 0.36$  at 1.3 K. Here the bias current ranges from 50 to 70  $\mu\text{A}$ .

using room-temperature amplifiers [1,58]. The use of a low-temperature current amplifier [9], while voltage biasing the  $\mu$ -SQUID, is expected to further improve the sensitivity.

## VI. CONCLUSION

In conclusion, we discussed the crossover from the fully overheated WL, i.e., the SBT regime, where the supercurrent is either on or off, to the (isothermal) RSJ case, where the supercurrent contribution decays progressively when the bias current exceeds the critical current. This physics is relevant not only for WLs but also for Josephson junctions based on nanowires, two-dimensional materials, and topological insulators, where a large supercurrent density can appear, implying a large power density at the resistive switch, together with poor heat evacuation, thus creating hysteresis. A single parameter  $\beta$  reflects the balance between the heat evacuation from the WL and the injected heat; it can be tuned by trimming the critical current and/or varying the thermal coupling to the bath. This balance determines the amplitude of voltage modulation in the phase dynamic regime. In terms of applications at low temperature, the existence of voltage oscillations makes hysteretic  $\mu$ -SQUIDS useful as flux-to-voltage transducers for probing magnetism at the nanoscale with a wide bandwidth.

## ACKNOWLEDGMENTS

We are indebted to T. Crozes for help in device fabrication at the Nanofab platform at Néel Institute. Help from A. Duley in calculating the current-phase relation is thankfully acknowledged. S.B. acknowledges financial support from CSIR, government of India. A.K.G. acknowledges a research grant from the SERB-DST of the government of India. A.K.G. also thanks Université Grenoble Alpes for a visiting position. C.B.W. and H.C. acknowledge financial support from the LabEx LANEF (ANR-10-LABX-51-01) project ÔUHV-NEQÓ. We acknowledge financial support from Centre Franco-Indien pour la promotion de la Recherche Avancée (CEFIPRA) through project 5804-2.

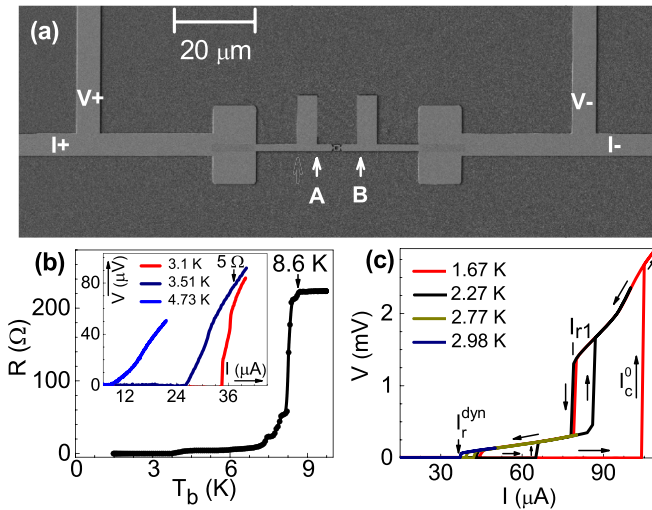


FIG. 7. (a) Larger-area SEM image of the  $\mu$ -SQUID showing the current and voltage leads. (b)  $R$ - $T_b$  plot at a fixed  $I = 10 \mu\text{A}$  showing the superconducting transition at an onset temperature of 8.6 K. The inset shows some IVCs in the nonhysteretic regime. (c) Hysteretic IVCs over a larger range of bias current showing thermal instability at  $I_{r1}$ .

#### APPENDIX A: ADDITIONAL EXPERIMENTAL DATA

Figures 7(a) and 7(b) show the large-scale scanning electron microscope (SEM) image of the  $\mu$ -SQUID together with its resistance versus bath temperature ( $R$ - $T_b$ ) curve and nonhysteretic IVCs. The WL  $T_c$  of 6 K cannot be found from the  $R$ - $T_b$  plot as the bias current of  $10 \mu\text{A}$  is too high.

Figure 7(c) shows hysteretic  $I$ - $V$  characteristics over a large bias range. We see multiple retrapping currents, with the larger-magnitude ones representing thermal instabilities in wider portions [see arrows labeled A and B in Fig. 7(a)] of the device, as evidenced by the resistance values above the respective retrapping currents. The physics of thermal instability at higher bias currents [above  $I_{r1}$ ; see Fig. 7(c)] beyond the dynamic regime was already reported by some of us [27,31].

Figure 8(a) shows the  $dV/dI$ - $I$  plots for the first device at four different temperatures to depict the saturation to the linear IVC for bias currents beyond  $I_h$ . Figure 8(b) depicts

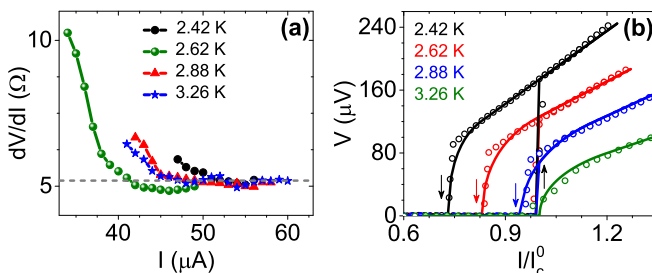


FIG. 8. (a) The variation of the differential resistance  $dV/dI$  with  $I$  in the range  $I_r^{\text{dyn}} < I$ . The dotted line shows the saturation to  $R_N \approx 5.2 \Omega$  for  $I \geq I_h$ . (b) Zero-field IVCs (symbols) and the fits (solid lines) to the DTM. Fitted  $\beta$  values are 1.45, 1, 0.75, and 0.65 for  $T_b = 2.42, 2.62, 2.88,$  and  $3.26$  K, respectively.

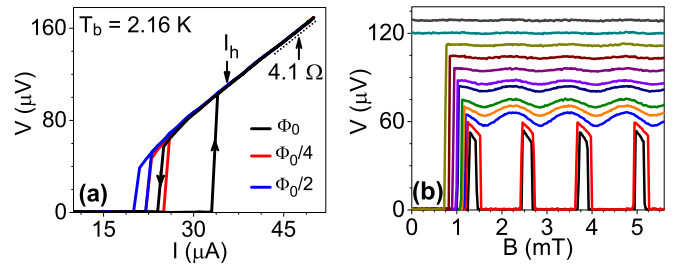


FIG. 9. (a)  $I_r^{\text{dyn}}$  oscillation with  $B$  at  $T_b = 2.16$  K for a third  $\mu$ -SQUID with  $T_h = 2.75$  K. (b)  $V$ - $B$  oscillations at this temperature for  $I = 25$  to  $38 \mu\text{A}$ .

the fits of the experimental zero-field IVCs to the DTM at four different temperatures after incorporating an appropriate excess current [20] defined as the intercept of the extrapolated linear Ohmic branch on the current axis. The latter, as well as the reduced  $I_c$  modulation with flux as discussed earlier, is beyond the DTM and is believed to arise from nonideal WL behavior.

Similar results on transport measurements observed in another (third)  $\mu$ -SQUID are shown in Figs. 9(a) and 9(b). The crossover temperature  $T_h$  of this device is found to be 2.75 K. In the hysteretic regime (below 2.75 K), the retrapping current  $I_r^{\text{dyn}}$  oscillates along with  $I_c$  with  $B$  [see Fig. 9(a) for  $T_b = 2.16$  K]. The estimated resistance from the linear Ohmic branch of IVCs beyond  $I_h$  is  $4.1 \Omega$ . The period of oscillation is the same, i.e., 1.25 mT, as that of the first device. The  $V$ - $B$  oscillations at 2.16 K are shown in Fig. 9(b) for bias currents ranging from  $I = 25$  to  $38 \mu\text{A}$ .

#### APPENDIX B: NONSINUSOIDAL $I_s(\varphi)$ RELATION AND $I_c$ MODULATION

As opposed to the short ( $\ell \ll \xi$ ) WLs, where the supercurrent phase  $I_s(\varphi)$  relation is sinusoidal ( $I_s = I_c \sin \varphi$ ) [57], the longer WLs ( $\ell \geq \xi$ ) exhibit a nonsinusoidal  $I_s(\varphi)$ . Using Ginzburg-Landau theory (which is valid close to  $T_c$ ), the  $I_s(\varphi)$  relation for a single WL of different lengths is calculated and shown in Fig. 10 [54]. For a SQUID with identical WLs, the magnetic flux  $\Phi$  gives rise to a phase difference  $2\pi\Phi/\Phi_0$  between the two WLs. Adding the two WL's supercurrents with this phase difference, we obtain the total supercurrent  $I_s$ . Figure 10(b) shows the total  $I_s$  as a function of  $\varphi$  at  $\Phi = \Phi_0/2$ .

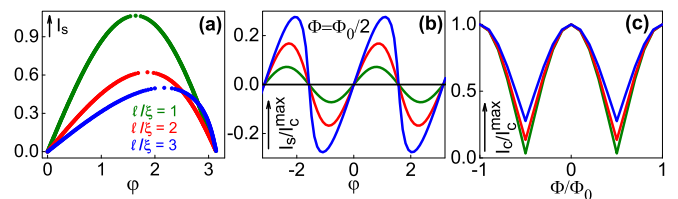


FIG. 10. (a)  $I_s(\varphi)$  relation for different  $\ell/\xi$  values. For  $\ell/\xi \geq 4$ ,  $I_s$  is no longer single valued. (b)  $I_s/I_c^{\text{max}}$  as a function of  $\varphi$  at  $\Phi = \Phi_0/2$ . Here  $I_c^{\text{max}}$  is the SQUID critical current at zero flux. (c)  $I_c/I_c^{\text{max}}$  variation with flux. The green, red, and blue curves represent  $\ell/\xi = 1, 2,$  and  $3$ , respectively. The black line in (b) shows  $I_s$  for the perfectly sinusoidal  $I_s(\varphi)$  relation at  $\Phi = \Phi_0/2$ .

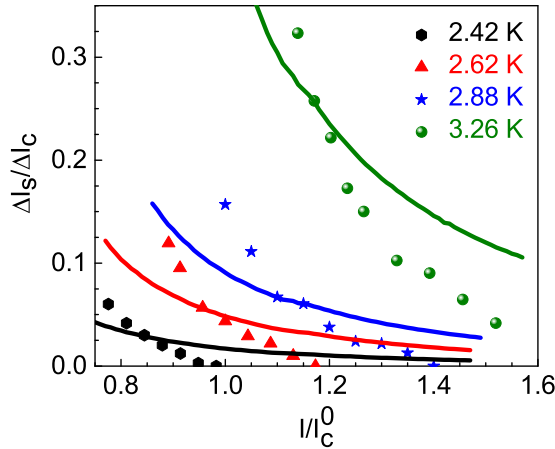


FIG. 11. Variation of residual supercurrent  $\Delta I_s/\Delta I_c$  in the resistive branch at  $T_b = 2.42, 2.62, 2.88,$  and  $3.26$  K as calculated from experimental data (shown by symbols). Solid lines represent the best fit to the RCSJ model.  $I_c^0$  on the x axis is the critical-current value at zero flux for respective  $T_b$ .

For a short WL-based SQUID, with perfectly sinusoidal  $I_s(\varphi)$ , this total  $I_s$  at  $\Phi = \Phi_0/2$  is identically zero, which is clearly not the case for long WL-based SQUIDS.

Figure 10(c) shows the  $I_c(\Phi)$  oscillations for  $\ell/\xi = 1, 2,$  and  $3$ , with  $I_c^{\max}$  being the maximum (with respect to  $\varphi$ ) value of  $I_s$  at a given  $\Phi$ . The  $I_c$  modulation amplitude decreases with increasing  $\ell/\xi$ . This demonstrates how the  $I_c$  modulation of a SQUID with flux is limited by the nonsinusoidal  $I_s(\varphi)$  relation of the WLs.

### APPENDIX C: RCSJ MODEL

Here we attempt the fitting of the supercurrent relative modulation  $\Delta I_s/\Delta I_c$  with the RCSJ model. This is not very

plausible due to the lack of sharp cutoff in  $I_s$ , which is quite apparent in the experiments.

TABLE II. Comparison of measured  $I_r^{\text{dyn}}$  and  $I_c^0$  with calculated (from  $I_r^{\text{dyn}}$  data) and fitted  $\beta_c$  for different temperatures.

$T_b$ (K)	$I_c^0$ ( $\mu\text{A}$ )	$I_r^{\text{dyn}}$ ( $\mu\text{A}$ )	Calculated $\beta_c$	Fitted $\beta_c$
2.42	58	44	2.13	5.4
2.62	46	40	1.5	3.2
2.88	40	38	0.8	2.33
3.26	31.6	31.6		1.0

According to the RCSJ model [17], the current  $I$ , as shared between resistances, capacitances, and the Josephson junctions of the SQUID, can be written as

$$I = I_c^0 \sin \varphi + \frac{\mathcal{V}(t)}{R_N} + C \frac{d\mathcal{V}(t)}{dt}. \quad (\text{C1})$$

Here  $2R_N$  and  $C/2$  are the resistance and capacitance of each of the two junctions. We have again assumed the screening parameter  $LI_c^0/\Phi_0 \ll 1$ . Using the same dimensionless quantities as in Sec. I, we get

$$i = \sin \varphi + \dot{\varphi} + \beta_c \ddot{\varphi}. \quad (\text{C2})$$

Here  $\beta_c = \frac{2\pi}{\Phi_0} I_c^0 R_N^2 C$  is the effective Stewart-McCumber parameter for the SQUID.

We get the IVCs from the numerical steady-state solutions of Eq. (C2) and  $V = \Phi_0 \dot{\varphi}/2\pi$ . Using these solutions, we find that  $I_r^{\text{dyn}}/I_c^0$  depends on  $\beta_c$ . This fact is used to extract the  $\beta_c^{\text{calc}}$  values for experimentally measured  $I_r^{\text{dyn}}/I_c^0$ . Using the expression  $I_s = I - V/R_N$ , we have tried to fit the measured  $\Delta I_s/\Delta I_c$  to the RCSJ model in Fig. 11. The fitted  $\beta_c$  values are listed in Table II together with the values extracted from the values of the dynamic retrapping current  $I_r^{\text{dyn}}$ . We see from the fit that RCSJ does not fit well compared to the DTM.

[1] C. Granata and A. Vettoliere, Nano superconducting quantum interference device: A powerful tool for nanoscale investigations, *Phys. Rep.* **614**, 1 (2016).  
 [2] M. J. Martínez-Pérez and D. Koelle, NanoSQUIDS: Basics & recent advances, *Phys. Sci. Rev.* **2**, 20175001 (2017).  
 [3] W. Wernsdorfer, Single nanoparticle measurement techniques, *J. Appl. Phys.* **87**, 5094 (2000).  
 [4] W. Wernsdorfer, Classical and quantum magnetization reversal studied in nanometer-sized particles and clusters, *Adv. Chem. Phys.* **118**, 99 (2001).  
 [5] R. Piquerel, O. Gaier, E. Bonet, C. Thirion, and W. Wernsdorfer, Phase Dependence of Microwave-Assisted Switching of a Single Magnetic Nanoparticle, *Phys. Rev. Lett.* **112**, 117203 (2014).  
 [6] M. J. Martínez-Pérez, B. Müller, D. Schwebius, D. Korinski, R. Kleiner, J. Sese, and D. Koelle, NanoSQUID magnetometry of individual cobalt nanoparticles grown by focused electron beam induced deposition, *Supercond. Sci. Technol.* **30**, 024003 (2017).  
 [7] C. Veauvy, K. Hasselbach, and D. Mailly, Scanning  $\mu$ -superconduction quantum interference device force microscope, *Rev. Sci. Instrum.* **73**, 3825 (2002).

[8] A. Finkler, Y. Segev, Y. Myasoedov, M. L. Rappaport, L. Ne'eman, D. Vasyukov, E. Zeldov, M. E. Huber, J. Martin, and A. Yacoby, Self-aligned nanoscale SQUID on a tip, *Nano. Lett.* **10**, 1046 (2010).  
 [9] D. Vasyukov, Y. Anahory, L. Embon, D. Halbertal, J. Cuppens, L. Neeman, A. Finkler, Y. Segev, Y. Myasoedov, M. L. Rappaport, M. E. Huber, and E. Zeldov, A scanning superconducting quantum interference device with single electron spin sensitivity, *Nat. Nanotechnol.* **8**, 639 (2013).  
 [10] L. Chen, H. Wang, X. Liu, L. Wu, and Z. Wang, A high-performance nb nano-superconducting quantum interference device with a three-dimensional structure, *Nano. Lett.* **16**, 7726 (2016).  
 [11] J. E. Duvauchelle, A. Francheteau, C. Marcenat, F. Chiodi, D. Débarre, K. Hasselbach, J. R. Kirtley, and F. Lefloch, Silicon superconducting quantum interference device, *Appl. Phys. Lett.* **107**, 072601 (2015).  
 [12] R. Wolbing, J. Nagel, T. Schwarz, O. Kieler, T. Weimann, J. Kohlmann, A. Zorin, M. Kemmler, R. Kleiner, and D. Koelle, Nb nano superconducting quantum interference devices with high spin sensitivity for operation in magnetic fields up to 0.5 T, *Appl. Phys. Lett.* **102**, 192601 (2013).

- [13] S. Mandal, T. Bautze, O. A. Williams, C. Naud, E. Bustarret, F. Omnès, P. Rodière, T. Meunier, C. Bauerle, and L. Saminadayar, The diamond SQUID, *ACS Nano*, **5**, 7144 (2011).
- [14] T. Schwarz, J. Nagel, R. Wölbing, M. Kemmler, R. Kleiner, and D. Koelle, Low-noise nano superconducting quantum interference device operating in tesla magnetic fields, *ACS Nano*, **7**, 844 (2013).
- [15] R. Russo, E. Esposito, A. Crescitelli, E. Di Gennaro, C. Granata, A. Vettoliere, R. Cristiano, and M. Lisitskiy, NanoSQUIDs based on niobium nitride films, *Supercond. Sci. Technol.* **30**, 024009 (2017).
- [16] A. Ronzani, C. Altimiras, and F. Giazotto, Highly Sensitive Superconducting Quantum-Interference Proximity Transistor, *Phys. Rev. Appl.* **2**, 024005 (2014).
- [17] *The SQUID Handbook*, edited by J. Clarke and A. I. Braginski (Wiley-VCH Verlag GmbH & Co. KGaA, Weinheim, 2004).
- [18] M. Tinkham, *Introduction to Superconductivity*, 2nd ed. (McGraw-Hill, New York, 1996).
- [19] W. J. Skocpol, M. R. Beasley, and M. Tinkham, Self-heating hotspots in superconducting thin-film microbridges, *J. Appl. Phys.* **45**, 4054 (1974).
- [20] M. Tinkham, J. U. Free, C. N. Lau, and N. Markovic, Hysteretic I-V curves of superconducting nanowires, *Phys. Rev. B* **68**, 134515 (2003).
- [21] H. Courtois, M. Meschke, J. T. Peltonen, and J. P. Pekola, Origin of Hysteresis in a Proximity Josephson Junction, *Phys. Rev. Lett.* **101**, 067002 (2008).
- [22] D. Hazra, L. M. A. Pascal, H. Courtois, and A. K. Gupta, Hysteresis in superconducting short weak links and  $\mu$ -SQUIDs, *Phys. Rev. B* **82**, 184530 (2010).
- [23] T. Schwarz, R. Wölbing, C. F. Reiche, B. Müller, M. J. Martínez-Pérez, T. Mühl, B. Büchner, R. Kleiner, and D. Koelle, Low-Noise YBa<sub>2</sub>Cu<sub>3</sub>O<sub>7</sub> Nano-SQUIDs for Performing Magnetization-Reversal Measurements on Magnetic Nanoparticles, *Phys. Rev. Appl.* **3**, 044011 (2015).
- [24] R. Arpaia, M. Arzeo, S. Nawaz, S. Charpentier, F. Lombardi, and T. Bauch, Ultra low noise YBa<sub>2</sub>Cu<sub>3</sub>O<sub>7- $\delta$</sub>  nano superconducting quantum interference devices implementing nanowires, *Appl. Phys. Lett.* **104**, 072603 (2014).
- [25] E. Y. Cho, Y. W. Zhou, J. Y. Cho, and S. A. Cybart, Superconducting nano Josephson junctions patterned with a focused helium ion beam, *Appl. Phys. Lett.* **113**, 022604 (2018).
- [26] V. V. Baranov, A. G. Balanov, and V. V. Kabanov, Dynamics of resistive state in thin superconducting channels, *Phys. Rev. B* **87**, 174516 (2013).
- [27] N. Kumar, C. B. Winkelmann, S. Biswas, H. Courtois, and A. K. Gupta, Controlling hysteresis in superconducting constrictions with resistive shunt, *Supercond. Sci. Technol.* **28**, 072003 (2015).
- [28] S. K. H. Lahm and D. L. Tilbrook, Development of a niobium nanosuperconducting quantum interference device for the detection of small spin populations, *Appl. Phys. Lett.* **82**, 1078 (2003).
- [29] G. Kimmel, A. Glatz, and I. S. Aranson, Phase slips in superconducting weak links, *Phys. Rev. B* **95**, 014518 (2017).
- [30] N. Shah, D. Pekker, and P. M. Goldbart, Inherent Stochasticity of Superconductor-Resistor Switching Behavior in Nanowires, *Phys. Rev. Lett.* **101**, 207001 (2008).
- [31] N. Kumar, T. Fournier, H. Courtois, C. B. Winkelmann, and A. K. Gupta, Reversibility of Superconducting Nb Weak Links Driven by the Proximity Effect in a Quantum Interference Device, *Phys. Rev. Lett.* **114**, 157003 (2015).
- [32] D. Hazra, J. R. Kirtley, and K. Hasselbach, Retrapping Current in Bridge-Type Nano-SQUIDs, *Phys. Rev. Appl.* **4**, 024021 (2015).
- [33] L.-K. Wang, D.-J. Hyun, and B. S. Deaver, Heating and flux flow in niobium variable-thickness bridges, *J. Appl. Phys.* **49**, 5602 (1978).
- [34] L.-K. Wang, A. Callegari, B. S. Deaver, D. W. Barr, and R. J. Mattauch, Microwave mixing with niobium variable thickness bridges, *Appl. Phys. Lett.* **31**, 306 (1977).
- [35] V. M. Krasnov, T. Golod, T. Bauch, and P. Delsing, Anticorrelation between temperature and fluctuations of the switching current in moderately damped Josephson junctions, *Phys. Rev. B* **76**, 224517 (2007).
- [36] L. Angers, F. Chiodi, G. Montambaux, M. Ferrier, S. Guéron, H. Bouchiat, and J. C. Cuevas, Proximity dc squids in the long-junction limit, *Phys. Rev. B* **77**, 165408 (2008).
- [37] A. Ronzani, M. Baillegerau, C. Altimiras, and F. Giazotto, Micro-superconducting quantum interference devices based on V/Cu/V Josephson nanojunctions, *Appl. Phys. Lett.* **103**, 052603 (2013).
- [38] Y. Song, Origin of capacitance in superconducting microbridges, *J. Appl. Phys.* **47**, 2651 (1976).
- [39] A. K. Gupta, N. Kumar, and S. Biswas, Temperature and phase dynamics in superconducting weak links, *J. Appl. Phys.* **116**, 173901 (2014).
- [40] J. Bardeen, Two-Fluid Model of Superconductivity, *Phys. Rev. Lett.* **1**, 399 (1958).
- [41] A. De Cecco, K. Le Calvez, B. Sacépé, C. B. Winkelmann, and H. Courtois, Interplay between electron overheating and ac Josephson effect, *Phys. Rev. B* **93**, 180505(R) (2016).
- [42] G. Berdiyrov, K. Harrabi, F. Oktasendra, K. Gasmi, A. I. Mansour, J. P. Maneval, and F. M. Peeters, Dynamics of current-driven phase-slip centers in superconducting strips, *Phys. Rev. B* **90**, 054506 (2014).
- [43] S. L. Chu, A. T. Bollinger, and A. Bezryadin, Phase slips in superconducting films with constrictions, *Phys. Rev. B* **70**, 214506 (2004).
- [44] M. W. Brenner, D. Roy, N. Shah, and A. Bezryadin, Dynamics of superconducting nanowires shunted with an external resistor, *Phys. Rev. B* **85**, 224507 (2012).
- [45] W. J. Skocpol, M. R. Beasley, and M. Tinkham, Phase-slip centers and nonequilibrium processes in tin microbridges, *J. Low Temp. Phys.* **16**, 145 (1974).
- [46] G. J. Dolan and L. D. Jackel, Voltage Measurements With Nonequilibrium Region Near Phase-Slip Centers, *Phys. Rev. Lett.* **39**, 1628 (1977).
- [47] Note that in the original paper introducing the DTM [39], we used a different notation,  $I_r^{\text{stat}}$ , for this current.
- [48] A. I. Gubin, K. S. Il'in, S. A. Vitusevich, M. Siegel, and N. Klein, Dependence of magnetic penetration depth on the thickness of superconducting Nb thin films, *Phys. Rev. B* **72**, 064503 (2005).
- [49] I. Charaev, T. Silbernagel, B. Bachowsky, A. Kuzmin, S. Doerner, K. Il'in, A. Semenov, D. Roditchev, D. Yu. Vodolazov, and M. Siegel, Proximity effect model of ultranarrow NbN strips, *Phys. Rev. B* **96**, 184517 (2017).

- [50] K. Il'in, D. Rall, M. Siegel, A. Engel, A. Schilling, A. Semenov, and H.-W. Huebers, Influence of thickness, width and temperature on critical current density of Nb thin film structures, *Phys. C (Amsterdam, Neth.)* **470**, 953 (2010).
- [51] L. N. Cooper, Superconductivity in the Neighborhood of Metallic Contacts, *Phys. Rev. Lett.* **6**, 689 (1961).
- [52] Ya. V. Fominov and M. V. Feigel'man, Superconductive properties of thin dirty superconductor-normal-metal bilayers, *Phys. Rev. B* **63**, 094518 (2001).
- [53] P. Dubos, H. Courtois, B. Pannetier, F. K. Wilhelm, A. D. Zaikin, and G. Schön, Josephson critical current in a long mesoscopic S-N-S junction, *Phys. Rev. B* **63**, 064502 (2001).
- [54] E. de Wolf and R. de Bruyn Ouboter, The Josephson supercurrent-phase relation, *Phys. B (Amsterdam, Neth.)* **176**, 133 (1992).
- [55] D. Hazra, J. R. Kirtley, and K. Hasselbach, Nano-superconducting quantum interference devices with suspended junctions, *Appl. Phys. Lett.* **104**, 152603 (2014).
- [56] K. Hasselbach, D. Mailly, and J. R. Kirtley, Micro-superconducting quantum interference device characteristics, *J. Appl. Phys.* **91**, 4432 (2002).
- [57] K. K. Likharev, Superconducting weak links, *Rev. Mod. Phys.* **51**, 101 (1979).
- [58] A. G. P. Troeman, H. Derking, B. Boerger, J. Pleikies, D. Veldhuis, and H. Hilgenkamp, NanoSQUIDs based on niobium constrictions, *Nano Lett.* **7**, 2152 (2007).
- [59] D. Pekker, A. Bezryadin, D. S. Hopkins, and P. M. Goldbart, Operation of a superconducting nanowire quantum interference device with mesoscopic leads, *Phys. Rev. B* **72**, 104517 (2005).